Strong winds and waves offshore

Larsén, Xiaoli Guo

Publication date:
2016

Document Version
Publisher's PDF, also known as Version of record

Strong winds and waves offshore

Xiaoli Guo Larsén

DTU Wind Energy E-0145
ISBN 978-87-93549-12-8
2016

Strong winds and waves offshore

Report DTU Wind Energy E-0145
2016

By Xiaoli Guo Larsén

Cover photo: [Text]
Published by: Department of Wind Energy, Frederiksborgvej 399
Request report from: www.dtu.dk
ISSN: [0000-0000] (electronic version)
ISBN: 978-87-93549-12-8 (electronic version)

ISSN: [0000-0000] (printed version)
ISBN: 978-87-93549-12-8 (printed version)

Contents

1 Preface

This report is prepared for Statoil, with the intention to introduce DTU Wind Energy's ongoing research activities on offshore extreme wind and wave conditions. The purpose is to share our recent findings and to establish possible further collaboration with Statoil.

The focus of this report is on the meteorological and oceanic conditions related to storm winds and waves over the North Sea. With regard to the offshore wind energy application, the parameters addressed here include: extreme wind and extreme waves, storm wind and waves and turbulence issues for offshore conditions.

2 Acknowledgement

The author acknowledges the support from Statoil. The results in this reports include contributions through publications from colleagues at DTU Wind Energy and DHI, among many, Søren Larsen, Jianting Du, Erik Petersen, Claire Vincent and Rodolfo Bolaños.

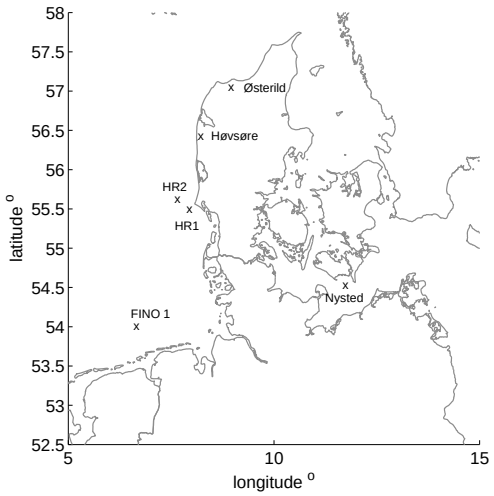

Figure 1: Locations of the sites where measurements are used in the analysis in this report. HR1 and HR2 are Horns Rev 1 mast 2 (M2) and Horns Rev 2 mast 8 (M8).

3 Introduction

For offshore wind energy functions such as operation, maintenance and design, good estimates of strong winds, waves and the statistics related are essential.

To develop our skills for such estimates is becoming one of the key research and development topics in the Wind Energy Department at DTU; one of our three departmental programs across sections is Offshore Wind Energy.

The key elements described in this report include a wind and wave coupled modeling system for modeling storms (sec. 4.1), the methodologies we developed for extreme wind and wave estimation (sec.s 4.2.2 and 4.2.1), as well as turbulence related to severe weathers at sea (sec. 5).

Our overall method is a combination of analysis of various types of measurements, such as met mast measurements, buoy, lidars, SAR data and cloud pictures, and modeling approaches such as numerical modeling and statistical modeling.

Figure 1 shows the locations of the met masts measurements analyzed in this report.

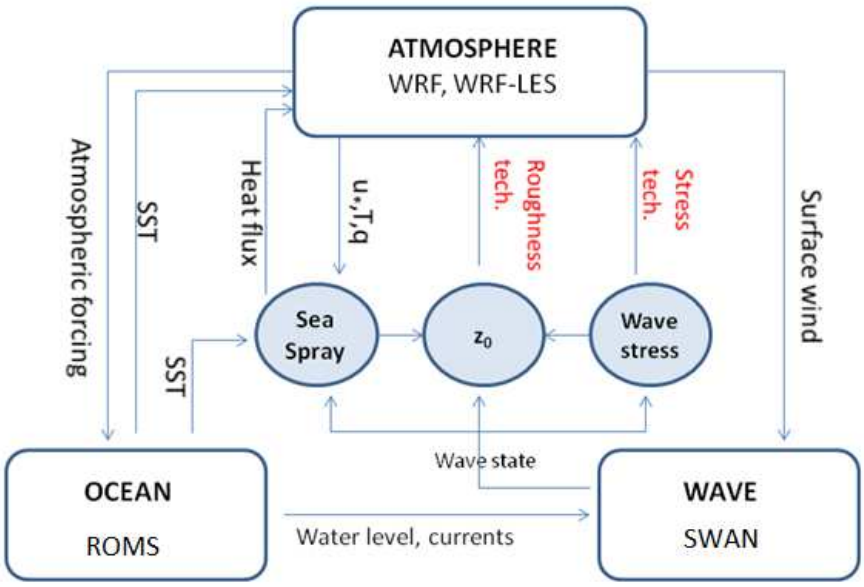

Figure 2: The diagram showing the components of the modeling system at DTU Wind Energy and approaches of coupling the components. From Project X-WiWa.

4 Extreme winds and waves

4.1 The wind-wave coupled modeling system

Within the ongoing ForskEL project X-WiWa (Extreme winds and waves for offshore turbines - coupling atmosphere and wave modeling for design and operation in coastal zones, 2013 - 2017), we developed modeling systems that couple the wave and atmospheric models, with special efforts on improving the modeling of coastal wind and wave conditions.

The modeling system developed at DTU Wind Energy uses the frame of the coupled-ocean-atmosphere-wave-sediment transport modeling system (COAWST) [1]. Currently we are using three model components in COAWST: Weather Research and Forecasting (WRF) model (www.wrf-model.org/index.php), the spectral wave model for near shore (SWAN) [2] and the Model Coupling Tookit (MCT). It is set that data exchange every 90 seconds between WRF and SWAN through MCT.

To introduce the wave impact to the atmospheric modeling, it is often through a description of the roughness length z_0 in terms of wave-related

parameters, similar to what is illustrated in Fig. 2 where the arrow pointing from wave model to the atmospheric model through z_0. Mostly, z_0 is described through the Charnock relation [3]:

$$z_0 = \alpha u_*^2/g \tag{1}$$

where α is the Charnock constant, and u_* is the frictional velocity and g is the gravitational acceleration.

DTU Wind Energy contributed to the modeling system in two ways. The first is the implementation and validation of many roughness length parameterizations to COWAST, including the schemes from Drennan et al. [4], Fan et al. [5], Liu et al. [6], Oost et al. [7] and Andreas et al. as in SWAN.

In the Drennan scheme, z_0 is parameterized through:

$$z_0 = 3.35 H_s (u_*/c_p)^{3.4} + 0.11\nu/u_* \tag{2}$$

where H_s is the significant wave height, ν is the viscosity coefficient and u_*/c_p is the reverse wave age, with c_p the wave phase velocity at the peak frequency of the wave spectrum. The second term of the right hand side of Eq. (2) describes the contribution from smooth flow to the roughness length, which is important only at very light winds.

The Fan scheme [5] includes the smooth flow contribution and a Charnock formulation base:

$$z_0 = \alpha u_*^2/g + 0.11\nu/u_* \tag{3}$$

where the Charnock parameter α is parameterized with the wave age c_p/u_*, with c_p the wave phase velocity at the peak frequency:

$$\alpha = a(c_p/u_*)^{-b} \tag{4}$$

where

$$a = \frac{0.023}{1.0568^{U_{10}}}, \qquad b = 0.012 U_{10} \tag{5}$$

where U_{10} is the wind speed at 10 m.

The Liu's scheme [6] has the same base format as Eq. (3) and here α is also parameterized through the wave age c_p/u_*, but in different form from the Fan-formulation Eq. (4), where for $0.35 < c_p/u_* < 35$:

$$\alpha = (0.085(c_p/u_*)^{3/2})^{1-1/\omega} (0.03 c_p/u_* \exp(-0.14 c_p/u_*))^{1/\omega} \tag{6}$$

and for $c_p/u_* > 35$

$$\alpha = 17.61^{1-1/\omega} 0.008^{1/\omega}, \tag{7}$$

where $\omega = \min(1, a_{cr}/(\kappa u_*))$, with a_{cr} =0.64 ms^{-1}.

Oost et al. [7] parameterizes z_0 in terms of wave length of the peak frequency and inverse wave age based on measurements from south North Sea:

$$z_0 = \frac{50}{2\pi} L_v (\frac{u_*}{c_p})^{4.5} + 0.11\nu/u_* \tag{8}$$

By default, the SWAN model used this expression:

$$z_0 = z \exp(-u_*/U_{10}) \tag{9}$$

where $z = 10$ m, and u_* and U_{10} are bounded by the following relationship:

$$u_* = 0.239 + 0.0433 \left((U_{10} - 8.271) + \sqrt{0.12(U_{10} - 8.271)^2 + 0.181} \right) \tag{10}$$

The above derivations are validated with measurements from various places representing open ocean conditions.

The Janssen scheme [8] differs from the above derivations since it does not use the derived parameters such as c_p, H_s or L_p. Rather, it uses the wave-induced stress that is calculated from the wind input through the wave balance equation:

$$z_0 = \frac{0.01 u_*^2}{g\sqrt{1 - \tau_w/\tau}} \tag{11}$$

Eq. (11) implies that when the wave-induced stress τ_w becomes comparable to the total stress in the surface layer, for instance in the presence of young wind sea, an enhancement in the Charnock value occurs, indicating an efficient momentum transfer from air to water.

All the above expressions, except for the Janssen formulation Eq. (11), are transformed into the relation of z_0 and U_{10} through measurements of wind, momentum and sensible heat fluxes from Horns Rev 1 M2 from year 1999 to 2005, and they are shown in Fig. 3. For moderate to strong winds, the Oost formulation, Eq. (8), gives the largest values of z_0. The Janssen formulation has also been reported to overestimate the stress and accordingly z_0, which was also experienced in our study. The consequence of using the Janssen or the Oost formulation is that the modeled winds are significantly smaller than using other schemes for z_0.

The spread of z_0 caused by the various z_0 parameterizations is comparable to the spread of z_0 obtained through measurements from various places. The $U_{10} - z_0$ relation from the simple Charnock formulation Eq. (1), as used in WRF, is inside the spread for the given wind speed range. In many cases, the

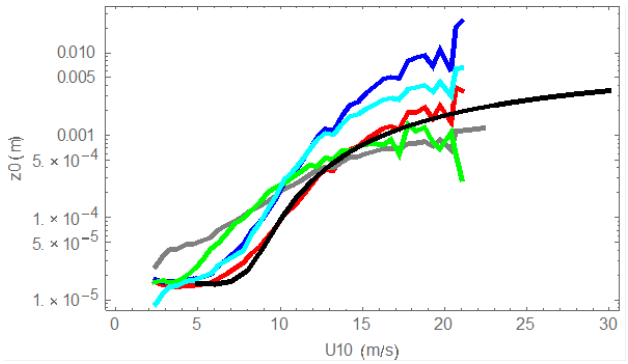

Figure 3: Roughness lengths calculated with data from Horns Rev with the following schemes: red - Drennen; gray - Fan; blue - Oost, green - Taylor-Yelland, cyan - Liu and black - SWAN.

z_0 estimates from these various schemes are of comparable magnitude and close to the Charnock parameterization, resulting in very small differences in wind speed. This has been interpreted by many as an indication that waves do not impact wind field. Here we prefer to interpret it as that the atmospheric modeling has not shown to be sensitive to the parameterization of z_0 when the magnitudes of z_0 from these parameterizations are similar to each other. The use of the Oost parameterization is seen to cause significant change in the wind field, but it is caused by the significantly larger magnitude of z_0, while not necessarily that the Oost parameterization feeds stronger wave impact to the atmospheric modeling.

It is not considered efficient to transfer the wave calculations to the atmospheric modeling through parameterizing z_0 in the manner described above. DTU Wind Energy developed an interface between the atmospheric and wave modeling, the so-called Wave Boundary Layer Model inside SWAN [9]. Here, the WBLM wind input source function explicitly calculates the drag coefficient based on momentum and kinetic energy conservation at the air-sea interface. Figure 4 shows the vertical distribution of the stress components and wind speed at $U_{10} = 10$ ms^{-1} and 40 ms^{-1}. The total stress, consists of turbulence stress and wave-induced stress, calculated in the WBLM is transferred to the atmospheric modeling. This corresponds to the second coupling approach illustrated in Fig. 2 where the arrow from wave model to the atmospheric model is marked with "stress". Our recently published study on ideal cases suggests that WBLM outperform the existing functions for wave modeling [9].

While this system can be used for forecasting as well as hindcasting in

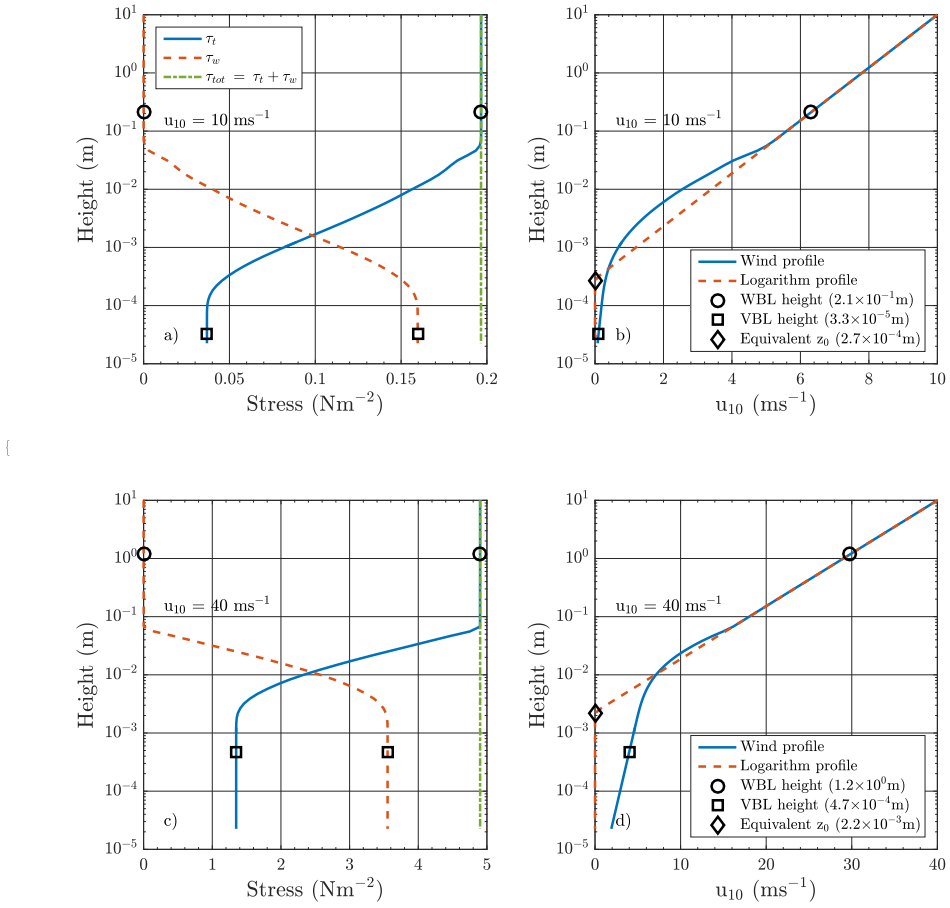

Figure 4: Vertical distribution of stress and wind profile in the wave boundary layer after 72 hours simulation at 3000 km fetch. (a) and (b) are for $u_{10} = 10$ ms^{-1}; (c) and (d) are for $u_{10} = 40$ ms^{-1}. From [9].

general, one of the main objectives of X-WiWa is to develop this coupled modeling system and apply it to produce extreme wind and extreme wave atlases for the Danish coastal waters. This will be done in connection with the selective dynamical downscaling method (SDDM). Hundreds of storms in the last three decades will be modeled at relatively high resolution to obtain the storm wind and wave fields that build the climatology of the extreme winds and waves for this region.

4.2 Extreme winds

4.2.1 The selective dynamical downscaling method

The selective dynamical downscaling method (SDDM) was developed at DTU Wind Energy to calculate the extreme wind atlas [10]. It uses mesoscale modeling, e.g. through WRF, to model decades' of individual storms that have affected a certain area. The storms that need to be modeled should also be related to the statistical methods for the estimation of the extreme winds. We choose to use the Annual Maximum Method (AMM) for the estimate of the T-year return wind. To identify these storms, we use existing modeled data that are of relatively coarse spatial and temporal resolutions, e.g. Climate Forecast System Reanalysis (CFSR) data, over the targeted area and identify, at each grid point in this area, the dates of the occurrence of the annual maximum wind. Before the relatively high resolution reanalysis (e.g. CFSR) became available, we have used the NCEP/NCAR reanalysis to calculate the geostrophic wind for the identification of the yearly strongest wind events. The identification of these storms is afterwards validated by point measurements. Following that, the mesoscale model is used to downscale these storms to a high resolution. The setup of the spatial resolution depends on the complexity of the terrain; e.g. we used 5 km for Denmark in [10] and 4 km for South Africa [11, 12]. When all storms are modeled, the annual wind maxima at each of the mesoscale grid point can be collected and they will be used to fit a Gumbel distribution to obtain the 50-year wind. In connection with further downscaling to microscales, here using the LINCOM model as embedded in WAsP Engineering (www.wasp.weng.dk), the individual wind maxima from the mesoscale grids are first corrected to a standard condition (at 10 m over a homogeneous surface with a z_0 of 5 cm). This is the so-called "generalization" procedure as used in the software WAsP family. Details about the generalization can be found in [10].

This method has been applied for calculating the extreme wind atlases for the North Sea [13], Denmark, Gulf of Suez [10] and South Africa [14]. Figures 5, 6, 7 and 8 are copies of the atlases from those studies.

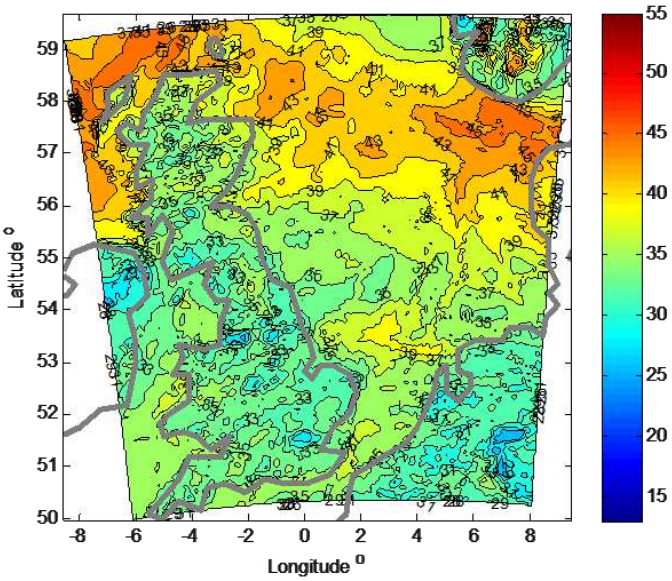

Figure 5: The atlas of the 50-year wind at 100 m over the North Sea using WRF modeling and the selective dynamical downscaling method. From [13].

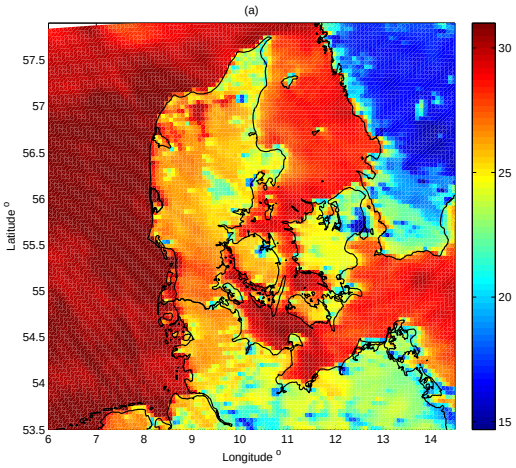

Figure 6: The atlas of the 50-year wind at 10 m over Denmark using WRF and the selective dynamical downscaling method. From [10].

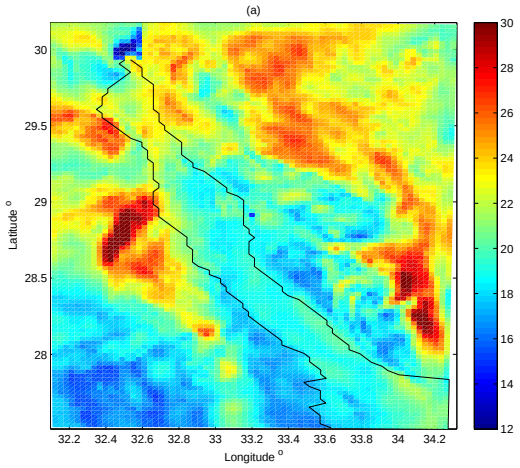

Figure 7: The atlas of the 50-year wind at 10 m over Gulf of Suez using WRF and the selective dynamical downscaling method. From [10].

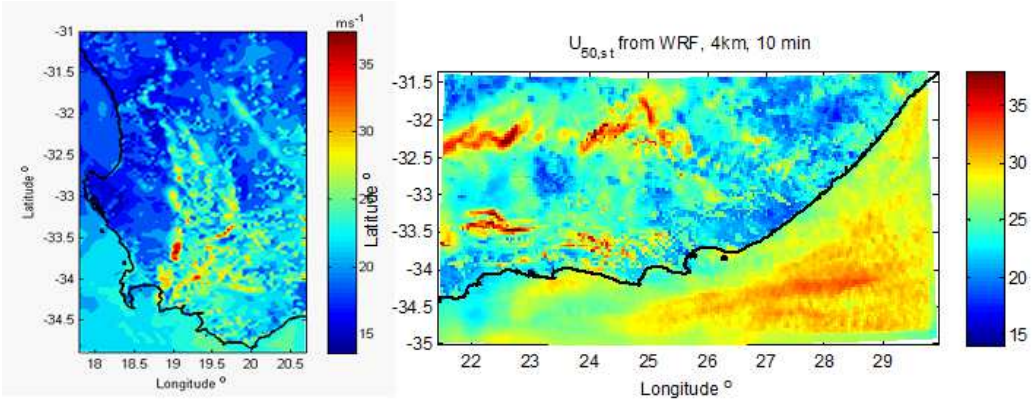

Figure 8: The atlas of the 50-year wind at 10 m with a roughness length of 5 cm over South Africa using WRF and the selective dynamical downscaling method. From [15].

In the above applications, the atmospheric model WRF has been used alone, without being coupled to a wave model.

For offshore applications, the modeling system introduced in sec 4.1 will be used. In connection with the Danish coastal extreme wind atlases, the CFSR data from 1979 to 2015 are used to identify the annual wind maxima at the CFSR grid points. About 500 storms are identified and will be downscaled. The modeling system should be able to provide not only storm wind but also storm waves. Following a series of studies on the storm Britta that occurred 30th Oct to 1st Nov 2006 over the North Sea, we used our modeling system to reproduce the same storm and analyzed the wind-wave interaction in the presence of open cell structures [16]. During this storm, FINO 1 experienced a 20-year return significant wave height, being about 10 m. The modeling system helped in interpreting the mechanism behind the occurrence of the rare event at FINO 1.

4.2.2 The spectral correction method

It is a common challenge in the calculation of the extreme wind or wave, that there often lacks long term data to represent the extreme wind or wave climate. Long term measurements are rarely available in most cases with the fast development of wind energy recently. On the other hand, numerical modeling becomes more and more easily accessible and there is a rather long list of modeled data freely available, including hindcasts, reanalysis and analysis from various weather and climate centers. These data cover a large area, and many of them are global. In addition, they are often decades long.

However, these modeled data do not automatically solve the problems associated with the samples needed for extreme wind or wave calculation. For winds simulated with global or mesoscale models, the variations are smeared in certain frequency and wave number ranges depending on the model nature and model resolution, because of the spatial and temporal averaging effects [17, 18, 19]. This is reflected in the spectral domain as the lower spectral energy level in comparison with measurements; Fig. 13 demonstrates such mesoscale spectral behaviors of wind speed at 10 m from three models that are well-used for wind studies in Northern Europe, in comparison with measurements from Horns Rev 1. Similar spectral behaviors are observed for the reanalysis data, with even more missing variation due to even coarser spatial and temporal resolutions [20].

The variation in the wind time series is important for the purpose of extreme wind estimation. Our earlier study [21] shows that the estimate of annual maxima $\overline{u}_{max} = \overline{U}_{max} - \overline{U}$, with $\overline{U}_{max}$ the mean of the annual maxima and $\overline{U}$ the mean wind, is a function of the zero and second-order spectral

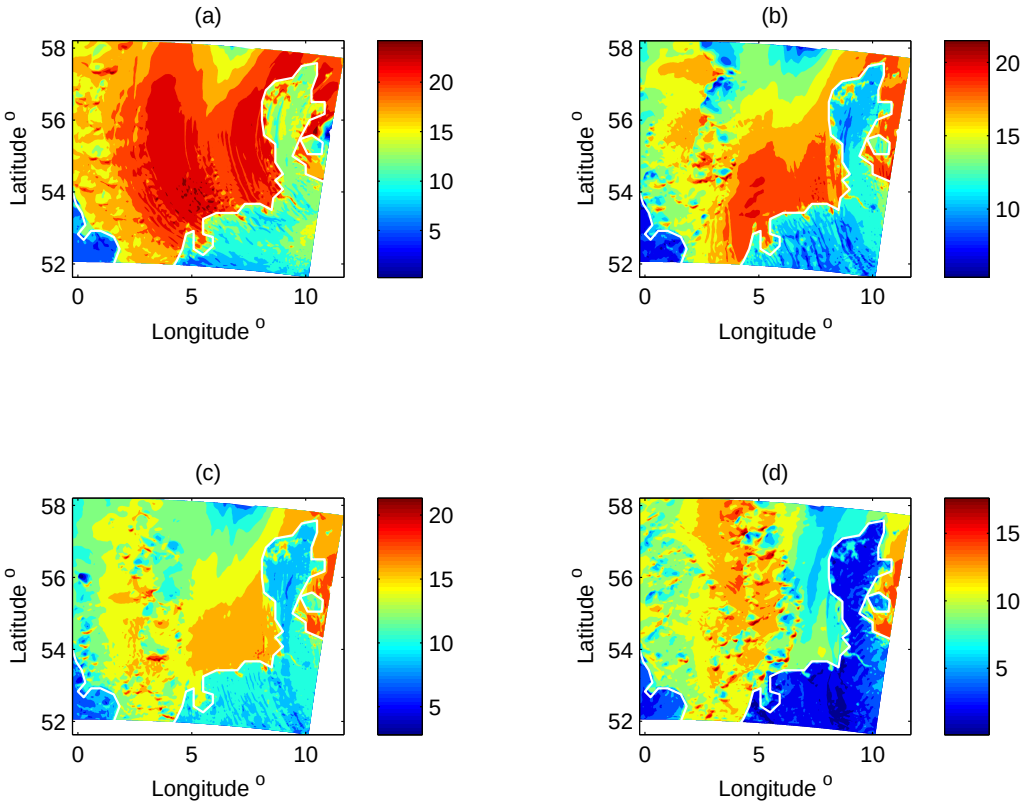

Figure 9: Modeled wind speed at 10 m on 2006-11-01, at (a) 4:00 (b) 10:00 (c) 13:00 and (d) 22:00, from the innermost model domain where the spatial resolution is 2 km. From [16].

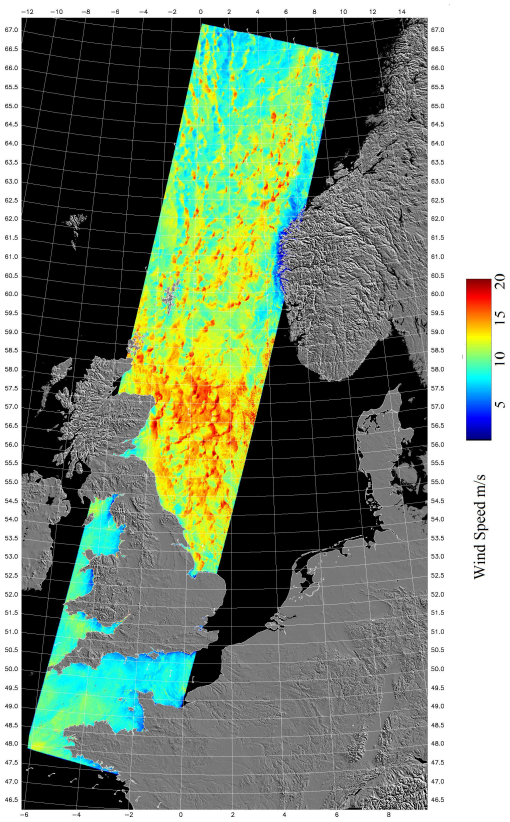

Figure 10: SAR wind speed at 10 m on 2006-11-01 10:26:41. From [16].

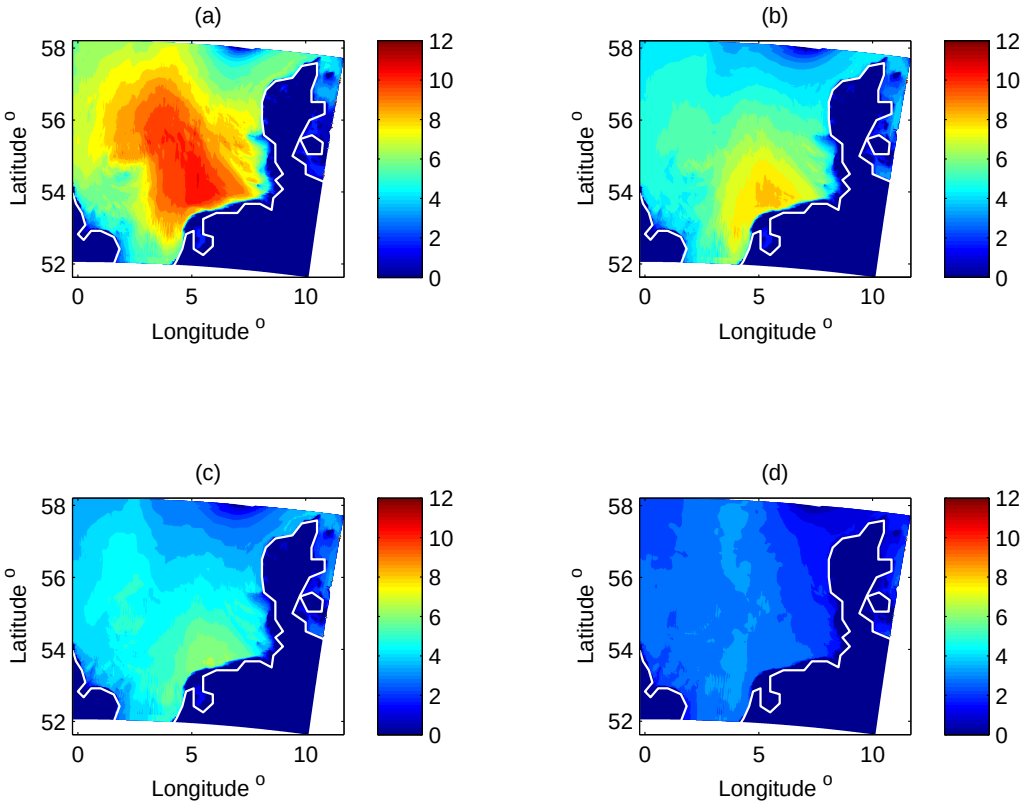

Figure 11: Modeled significant wave height on 2006-11-01, at the same time as Fig. 9. (a) 4:00 (b) 10:00 (c) 13:00 and (d) 22:00, from the innermost model domain. From [16].

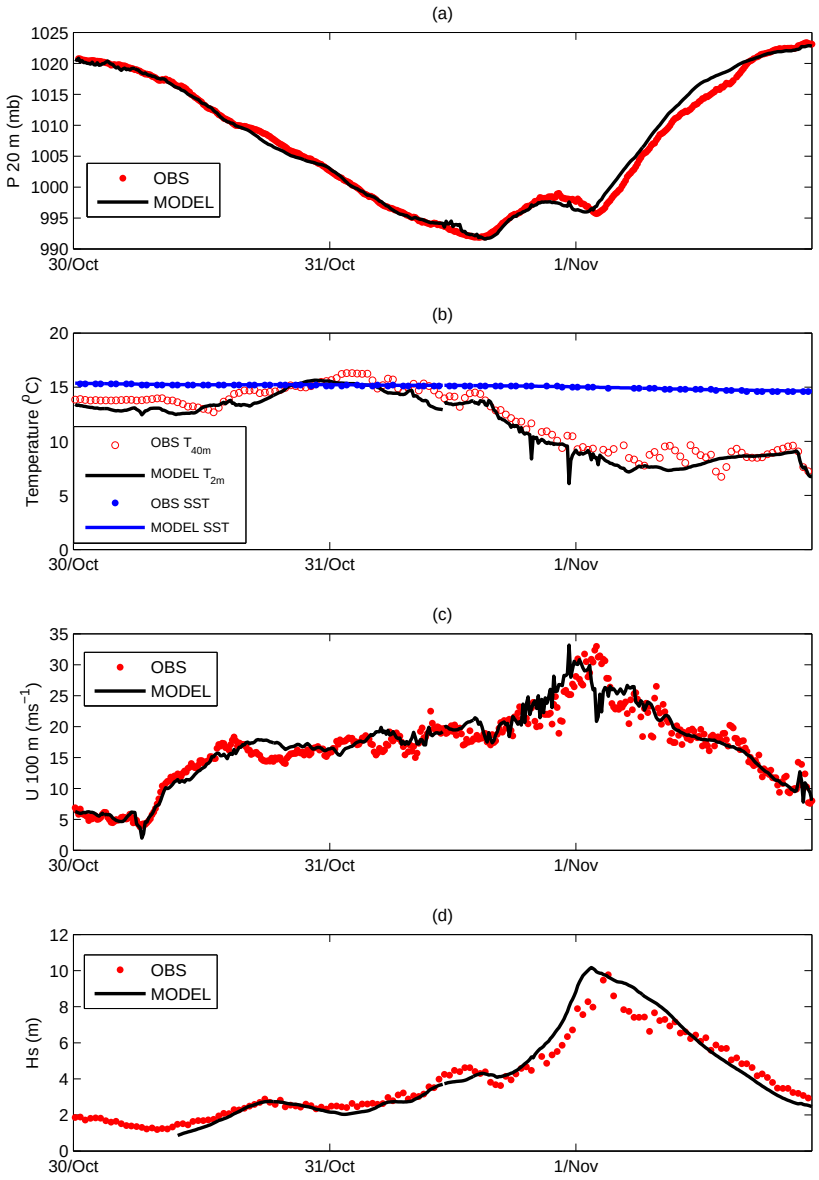

Figure 12: Modeled and measured time series at FINO 1 during 2006-10-30 00:00 and 2006-11-02 00:00. (a) pressure (b) temperatures (c) wind speed at 100 m (d) significant wave height H_s. From [16].

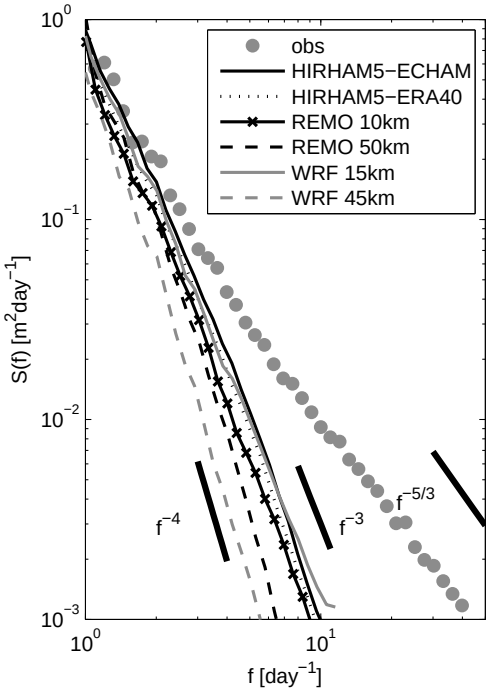

Figure 13: Spectra of wind speed at 10 m at Horns Rev from measurements and six model simulations, $S(f)$ vs frequency f. Thick short straight lines show the three reference slopes of $-5/3$, -3 and -4. From [21].

moment, m_0 and m_2:

$$\overline{u}_{max} = \sqrt{m_0}\sqrt{2\ln\left(\frac{1}{2\pi}\sqrt{\frac{m_2}{m_0}}T_0\right)} \tag{12}$$

where $T_0 = 1$ year, m_0 and m_2 are calculated with

$$m_j = 2\int_0^\infty \omega^j S(\omega) d\omega, \tag{13}$$

where $S(\omega)$ is the power spectrum of the Gaussian process $u(t)$, $\omega = 2\pi f$. The integration of Eq. (13) is done from $\omega = 0$ to $\omega = 2\pi(1/(2T_a))$, i.e. the upper limit of the integration becomes the Nyquist frequency. Thus, the integration does not diverge when the tails have slopes equal to or greater than -2.

Eq. (12) is derived under the assumption that the once-per-year exceedance F follows a Poisson process $F = \exp(-\lambda T_0)$, where λ is the rate of occurrence calculated with

$$\lambda = \int_0^\infty P(u,\dot{u})\dot{u}d\dot{u} = \frac{\sigma_{\dot{u}}}{\sqrt{2\pi}}P(u), \tag{14}$$

with $P(u,\dot{u})$ the conditional probability of u, $P(u)$ the probability of u, $\dot{u}$ the time derivatives of u, and it is assumed that u and $\dot{u}$ are independent. Here u is the wind speed minus its mean $(U - \overline{U})$. With a large threshold, such a distribution of the exceedance is valid for a Gaussian process for which

$$P(u) = \frac{1}{\sigma_u\sqrt{2\pi}}\exp\left(-\frac{u^2}{2\sigma_u^2}\right). \tag{15}$$

Note, in reality, the wind speed distribution follows rather a Weibull than a Gaussian distribution, which means that the assumption of u and $\dot{u}$ being independent could be questionable. Substituting Eq. (15) into (14) gives

$$\lambda = \frac{1}{2\pi}\frac{\sigma_{\dot{u}}}{\sigma_u}\exp\left(-\frac{u^2}{2\sigma_u^2}\right). \tag{16}$$

Equation (16) can be re-written as

$$\lambda = \frac{1}{2\pi}\sqrt{\frac{m_2}{m_0}}\exp\left(-\frac{u^2}{2m_0}\right). \tag{17}$$

For the maximum wind that occurs once a year, $\lambda T_0 = 1$, using this in Eq. (17) it gives Eq. (12).

The missing variation in the modeled wind time series in comparison with measured one shown in Fig. 13 in terms of power spectrum will lead to

underestimation in both m_0 and m_2, particularly in m_2, resulting in underestimation in u_{max}.

Measurements, even being only one year long, could be used to provide the wind variation in terms of the power spectral properties to compensate the missing information of the modeled data [22].

In the absence of measurements, a spectral model is recommended to be used from about 1 day up to about a resolution of 10 minutes:

$$S(f) = af^{-5/3} \tag{18}$$

where f is the frequency. The background and derivation of Eq. (18) are given in sec. 5.1.

We have used this method to produce the extreme wind atlas for South Africa in the South Africa Wind Atlas project [15], where the results have been validated with measurements from 70 stations across the country. This method is now being implemented in WAsP Engineering version 4 (www.wasp/weng) for the whole globe in connection with the use of two reanalysis data CFDDA (Climate Four Dimensional Data Assimilation) and CFSR.

4.3 Extreme waves

Similar to the climatological modeled wind time series, the wave height time series from most modeling also suffer from missing variation in the relatively high frequency range. Fig. 14a shows such an example for the FINO 1 site (Fig. 1) where the time series of the significant wave height was from WAM using wind input SKIRON; the spatial resolution is 5 km and the data length is 10 years. The model was performed by Athens University under the EU MARINA Platform project.

FINO 1 most represents an open sea, deep water condition. The variation of H_s is further complicated in the coastal shallow water zone where it has often been documented that models tend to overestimate mean values of H_s due to unresolved processes such as swell and shoaling [24, 25, 26]. This is also the case in [23], see their figures 6 for a number of storm cases at the Horns Rev 1 buoy (Fig. 1). The overestimation at Horns Rev is general, so that in the power spectrum there is an overestimation of the variance in the low frequency range, see Fig. 15a.

To calculate the spectral variables m_0 and m_2 for H_s, for the open water site FINO 1, only the high frequency part needs to be corrected (Fig. 14b). For the shallow water coastal site Horns Rev, first the low frequency part needs to be corrected and this can be done through a linear regression between the modeled and measured time series and the result is satisfactory, see Fig. 15a. Secondly the high frequency part needs to be corrected by

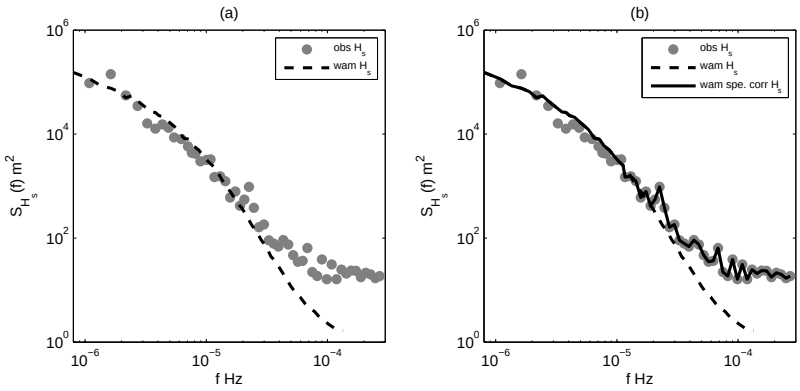

Figure 14: (a) Power spectra of measured and modeled significant wave height H_s at FINO 1. (b) Combination of the observed and modeled spectra to obtain the full spectrum (solid black curve), on top of (a). From [23].

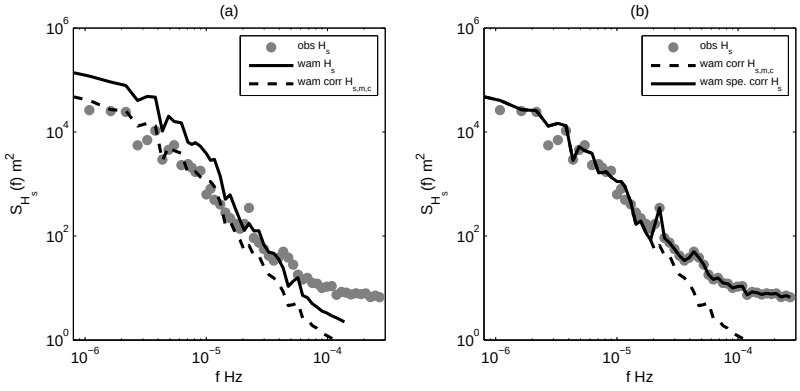

Figure 15: (a) Power spectra of measured and modeled significant wave height H_s at Horns Rev. (b) Combination of the observed and modeled spectra to obtain the full spectrum (solid black curve), on top of (a). From [23].

introducing the spectrum from measurements, and the result is the solid line in Fig. 15b.

The estimate of the 50-year return value of H_s at FINO 1 and Horns Rev by combining the modeled and measured data is satisfactory.

However, unlike the wind time series, we do not have an universal spectrum for H_s in the corresponding frequencies where model performance is not good.

In general one should have a wave model that can reproduce the wave statistics, not only for the open sea but also for the coastal areas.

In [16], the coupled modeling system has successfully reproduced H_s during the storm Britta at several sites, including FINO 1 (Fig. 12d).

5 Turbulence Issues Offshore

When it is said that the offshore environment is harsher for constructions than onshore conditions, the relevant parameters could be the stronger mean wind, the larger wind fluctuation accompanying the weather systems, currents, waves, etc. In the calculation of loads for turbines, turbulence intensity is an important parameter. In the absence of measurements, a turbulence model is used, such as the Kaimal model [27] and the Mann model [28] to calculate the spectral properties of the wind components. Such classical turbulence models are built on the assumption that the turbulence is surface driven. Under this concept, with the often used parameterizations of surface conditions over water, such as the roughness length, problems should seldom be expected regarding turbulence since the three dimensional turbulence level is in general low over water in comparison with land conditions.

As the modern wind turbines become hundreds of meters tall and the wind farms spreading tens, or even hundreds, of kilometers in space, the wind variations, described through local surface parameters only, become inaccurate since the contribution from flows of larger scales becomes non-negligible.

The following sub-sections collect our published as well as unpublished studies on turbulence covering synoptic scales, mesoscale and microscales.

5.1 The full scale spectrum of the boundary layer wind

In sec. 4.2.2, Eq. (18) was introduced to describe the wind speed spectrum in the range of about 1 day^{-1} to about 0.05 min^{-1} for the spectral correction of the modeled time series in the absence of measurements. Eq. (18) is a part of the following expression:

$$S(f) = a_1 f^{-5/3} + a_2 f^{-3} \tag{19}$$

where $a_1 = 3 \times 10^{-4}$ m^{2}s$^{-8/3}$ and $a_2 = 3 \times 10^{-11}$ m^{2}s^{-4}. Eq. (19) was first derived from [29] using long term wind measurements from two offshore sites, Horns Rev and Nysted (Fig. 1), where the -3 slope part of the spectrum corresponds to geostrophic turbulence, interpreted generally to be related to the baroclinic instability. Eq. (19) was shown to be valid for frequencies from about 0.05 min^{-1} to about 0.2 day^{-1}. The frequency 0.2 day^{-1} corresponds to the maximum spectral energy in the energy containing range and it can be shown to be related to the synoptic weather processes since the autocorrelation of the 10-min averaged wind speed turns to be zero at this scale.

This part of spectral energy as described in Eq. (19) is, as standard, ignored in calculating standard parameters such as turbulence intensity. In a standard approach, in the absence of measurements, wind variance is calculated from a turbulence model that is described by local surface parameters, such as the Kaimal model or the Mann model, which we call here as the 3D turbulence. As Kaimal and Finnigan [27] wrote: "Implicitly in the development of spectral forms in the energy containing range is the assumption that a spectal gap exists, separating boundary-layer turbulence from external fluctuations". The "external fluctuations" correspond to Eq. (19) and we call it the 2D turbulence.

The "external fluctuations" were addressed as "inactive turbulence" in [30]. [30] cited the idea proposed by [31] that the sum of the inactive turbulence and the 3D turbulence will give the observed spectrum in the gap region. With the establishment of the inactive turbulence through Eq. (19), we prove this idea to be realistic through the measurements from coastal sites Høvsøre and Østerild and an offshore site Horns Rev, from 10 m (Høvsøre) up to 241 m (Østerild) [32, 33]. Figures 16 and 17 show that the sum of the 3D turbulence (described through Kaimal format for $f < f_p$, where f_p is the peak frequency of the 3D turbulence, black dots) and the 2D turbulence (green lines) gives the red curve, which is very close to the spectrum from measurements (blue curve).

In [32], it was shown that there is a diurnal peak in the wind speed spectrum at Høvsøre at 10 m, and this peak becomes very weak at already 40 m and is invisible at 60 m or higher. This suggests that the Høvsøre met mast experiences overall offshore condition at elevation higher than 60 m. At Østerild, however, even at 241 m, the diurnal peak is still present [33], suggesting its land characteristics in general. Seemingly, both the spectral behaviours around the gap over land and over water, close to the surface or high up to 241 m, can be described in the same simple manner.

The spectra of the wind components are required in a number calculations in wind energy applications, including loads. Due to the increasing size of the modern wind turbines, it is speculated that the contribution from frequencies lower than 0.001 Hz may play a non-negligible role. This is however a topic seldom touched upon in the literatures. [32] collected "stationary" days from years 2012 and 2013 from Høvsøre when the directional change during one day is less than 50° and there are 100 days satisfying this condition. Winds from these 100 days are decomposed into the along and cross wind components, u and v. Figure 18 shows the spectra for the three components u, v and the vertical wind w. In the 3D inertial subrange, we observe that v and w have comparable levels of energy, both greater than that of u component, a classical behavior. Consistent with the classical 3D turbulence theory,

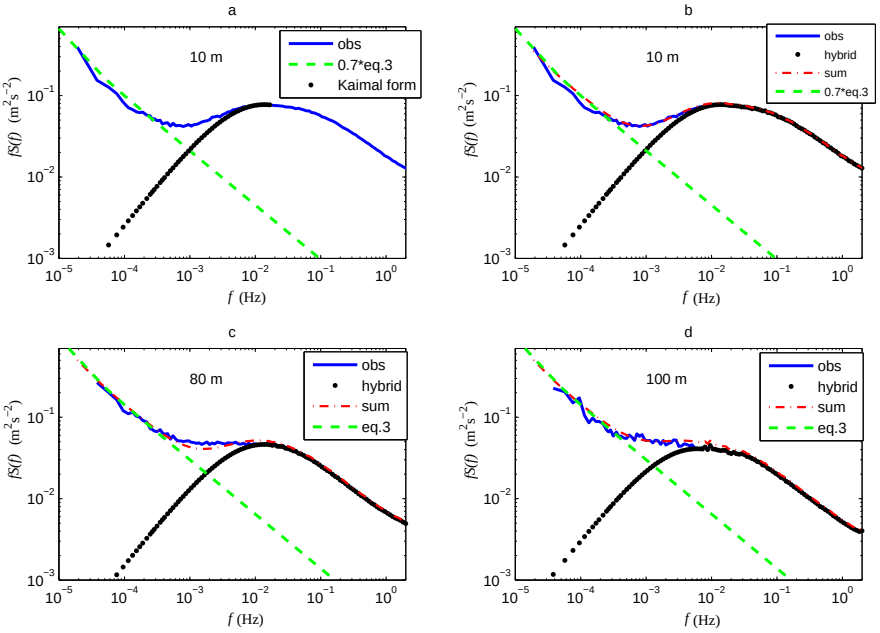

Figure 16: Superimpose of the spectral components. (a) at 10 m, measured spectrum together with the spectral model Eq. (18) multiplied by 0.7, extending to high frequencies, and a Kaimal spectrum for frequencies lower than the peak frequency. (b) at 10 m, the sum of the mesoscale spectrum with a slope of $-5/3$ and the microscale spectrum with the shape of a Kaimal model (the red curve) gives the observed spectrum. (c) The same as (b) but for 80 m. (d) The same as (b) but for 100 m. From [32].

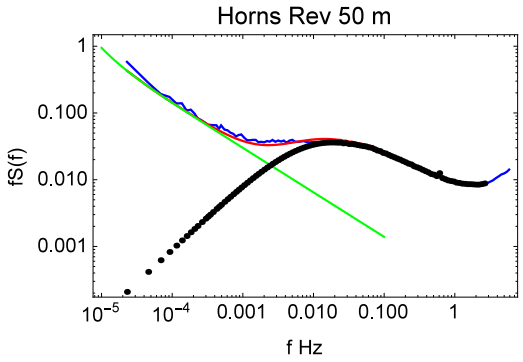

Figure 17: Similar to Fig. 16, but for Horns Rev 50 m.

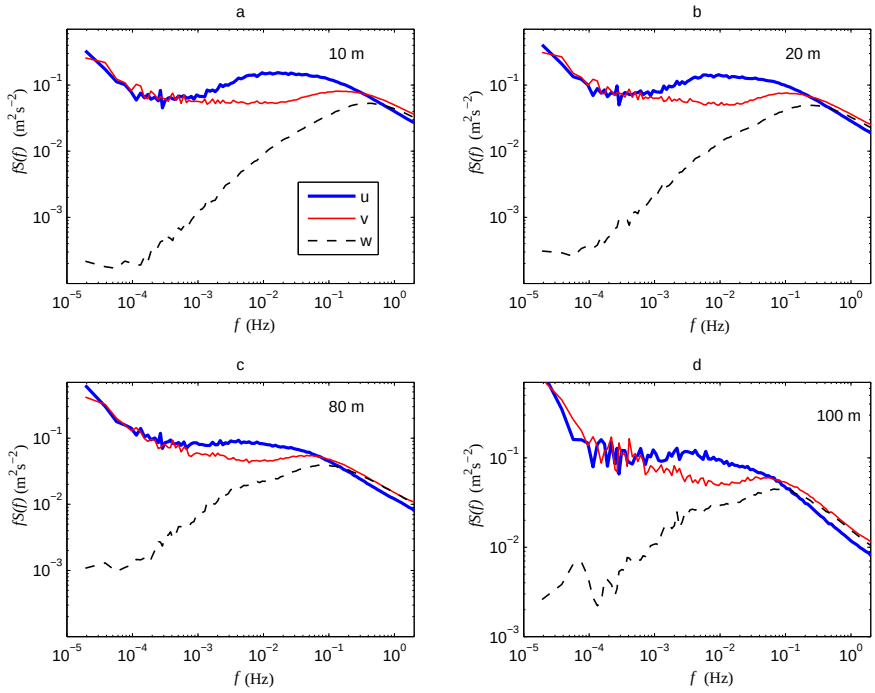

Figure 18: The three components u, v and w from where days where daily directional change is less than 50°. (a) 10 m; (b) 20 m; (c) 80 m; (d) 100 m. From [32].

the peak frequency for w is the highest, and for u it extends to the lowest frequencies. For v, $fS(f)$ levels off at an energy level extending from the 2D turbulence.

5.2 Storm wind spectrum

Strong winds over the North Sea are mostly associated with the frontal weathers. Accompanying the fronts, when specific meteorological conditions are satisfied, organized features are often observed over the sea and sometimes propagate over the land adjacent, such as mountainous gravity waves, boundary layer rolls and open cells.

The spectral analysis of the winds associated with these special weathers can provide a good picture of the corresponding turbulence. Such an analysis is being done here with a combination of measurements and numerical modeling. The following sections address, respectively, the turbulence characteristics related to fronts (sec. 5.2.1), boundary layer rolls (sec. 5.2.2), gravity waves (sec. 5.2.3) and open cells (sec. 5.2.4).

5.2.1 Fronts

The famous Van der Hoven spectrum [34] has been used by many as evidence that the spectral gap exists. This conclusion has been questioned lately since the high frequency region in the Van der Hoven spectrum was measurements during a passage of a hurricane. In comparison with the full-scale spectra from Høvsøre that are obtained from two years of data [32], the Van der Hoven spectrum does show a more striking gap as well as 3D turbulence peak at 100 m.

The wind speed spectra during frontal storms are expected to be different from the climatological one, but how different?

From the year 2015, nineteen storms are identified from the Høvsøre measurements, based on the criteria that the wind speed at 60 m exceeds 20 ms^{-1} and two consecutive such events are separated by one week. For the nineteen storms, 1-day long time series of the 10-min mean wind speed are used to calculate the "mesoscale" spectra and at the same time, 10-min long time series of 20 Hz sonic data are used to calculate the high frequency 3D spectra. Both the mesoscale and 3D turbulence spectra are shown in Fig. 19 for 10 m and 80 m, respectively. On the same plots, the one-year spectra for 2015 are also shown for the two heights, in red lines. The red lines are in very good agreement with the spectra obtained in [32] from 2012 and 2013 for $f < 10^{-3}$ Hz. For $f < 10^{-3}$ Hz, the black line is the mean value of the 19 gray lines for the nineteen storms and it overlaps with the red and blue curves, suggesting

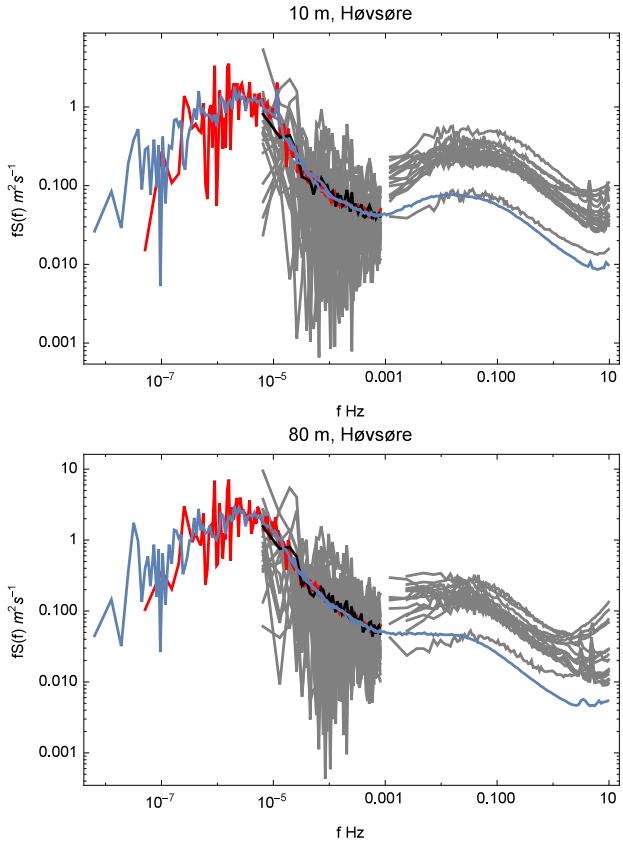

Figure 19: Spectra $fS(f)$ vs frequency f at Høvsøre. Gray curves: from 19 storms from 2015. Red: climatological spectrum from 10-min wind time series from 2015. Blue: climatological full-scale spectrum from 2012 and 2013 from [32]. (a) above: 10 m; (b) below: 80 m.

that for the mesoscale range, the mean of the storm spectrum follows the climatological value. For the high frequency range, where the spectrum is a function of the wind speed, surface roughness length and height, the storm spectra show higher energy level than the climatological one, resulting in more obvious spectral gap, both at 10 m and 80 m, as in the Van der Hoven spectrum.

We report here that the Kaimal model can satisfactorily describe the 3D turbulence for $10^{-3} < f < 1$ Hz. In all our plots with the sonic data, the uncertainty for $f > 1$ Hz is rather large and we disregard the results in that range.

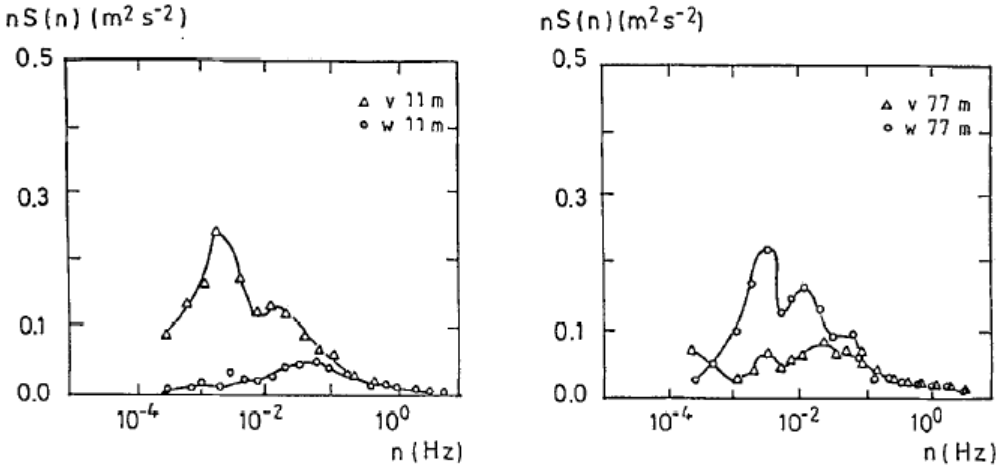

Figure 20: Examples of v and w-spectra measured at 11 m (left) and 77 m (right) in log-linear representation. Measurements are from Näsudden. From [36].

5.2.2 Boundary-layer rolls

In the atmospheric surface layer, the turbulence of a stationary and homogenous flow can be reasonably described by the classical turbulence theories such as Kaimal, Mann. These models seem having been able to perform reasonably well for the frontal strong wind as shown in sec 5.2.1. For these strong winds, stability effect becomes secondary. However, in the presence of the organized structures such as boundary-layer rolls, mountain gravity waves and open cells, these classical models often seem to be invalid for $f < f_p$ where f_p is the peak frequency of the 3D turbulence.

Figure 20 shows the contribution of the boundary layer rolls over the Baltic Sea to the spectral energy in v and w in the frequency range $2 \cdot 10^{-4} < f < 10^{-2}$ Hz, with a dominant peak at $f \sim 2 \cdot 10^{-3}$ Hz, whereas $fS(f)$ did not decrease to zero with decreasing frequency for $f < 10^{-2}$ Hz, as surface-layer turbulence theory would suggest.

[35] observed similar contribution from the boundary layer rolls that were developed when the cold icelandic air advected over the warmer Atlantic Ocean, except that the scales are even smaller, with peaks at around 0.025 Hz, see the copy of their Fig. 7 here in Fig. 21.

These observations suggest that the standard ways of calculating the atmospheric turbulence are embedded with uncertainties in the presence of the organized boundary layer rolls.

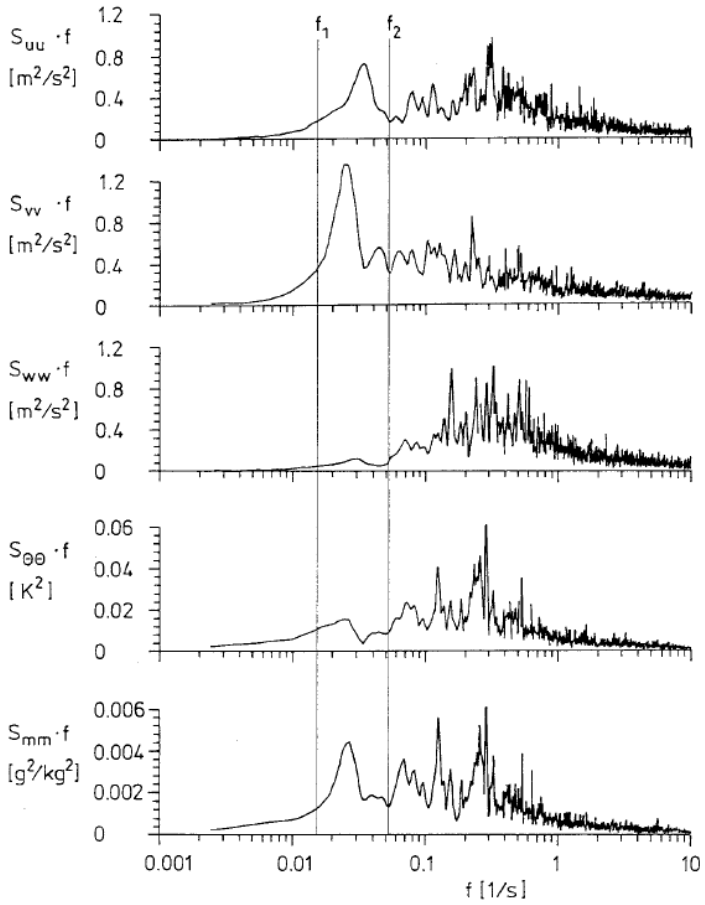

Figure 21: Variance spectra S_{aa} $(a = u, v, w, \theta, m)$ weighted by frequency f, where θ is the thermal temperature and m is the water vapor mixing ratio. f_1 and f_2 mark the limits of the roll-scale wavelength range. From [35].

5.2.3 Gravity waves

The gravity waves above the North Sea, as visible sometimes in the clouds or cloud pictures, or satellite data, are very likely generated by strong winds across the Scotland highlands or/and the Norwegian mountains, the so-called lee waves generated by the atmospheric uplift under stable atmospheric conditions.

[37] investigated the generation and development of such a case that was present above the North Sea and Denmark through SAR data, cloud pictures and WRF modeling, see Fig. 22 which is from [37]. The relevance of the gravity waves in wind energy application can be reflected in the spectral properties of the wind speed. [38] demonstrates that in the presence of gravity waves, the Doppler shift is significant and, without taking the Doppler effect into account, the Taylor hypothesis fails for the transformation between wave number k and the frequency f spectrum. In [38] the transformation was found to be robust when the Doppler shift was accounted for through the following equation:

$$\omega = \Omega + \mathbf{U}_0 \cdot \mathbf{k} = (\mathbf{c}_0 + \mathbf{U}_0) \cdot \mathbf{k} \tag{20}$$

([39]). Apparently, the Taylor transform is a special case with Doppler shift having $\Omega \to 0$:

$$\omega = \mathbf{U}_0 \cdot \mathbf{k}, \tag{21}$$

where ω is the wave frequency observed in a fixed system and thus $\omega = 2\pi f$. The magnitudes of the vectors $\mathbf{k}$ and $\mathbf{U}_0$ are k and U_0. Here, $\mathbf{U}_0 = \mathbf{U}_0(u_0, v_0)$, with u_0 and v_0 the zonal and meridional background wind speed, respectively. Figure 23 shows the success of including the Doppler shift in the transformation (Eq. (20), Fig. 23c and d) in the presence of gravity waves and the failure of not including the Doppler shift in the transformation (Eq. (21), Fig. 23a and b).

While the 2D flow has shown to be climatologically isotropic, it is not the case in the presence of organized structures. The dissimilarity between u and v as in Fig. 23 is an example. At the same time, the spatial coherence has also shown to be quite different for the along wind and cross wind component u and v. This is shown in [29], and here Fig. 24, through the analysis of 1 s time series from the gravity wave case at two met masts at Nysted M_1 and M_3, which are west-east oriented and the distance d is about 8 km, approximately 3/4 wave length. The u component, aligning with the wave propagation direction, fluctuates wavelike with the normalized frequency fd/U_0, with U_0 the wind speed at measurement height. u sometimes becomes entirely negatively correlated at the two masts. On the

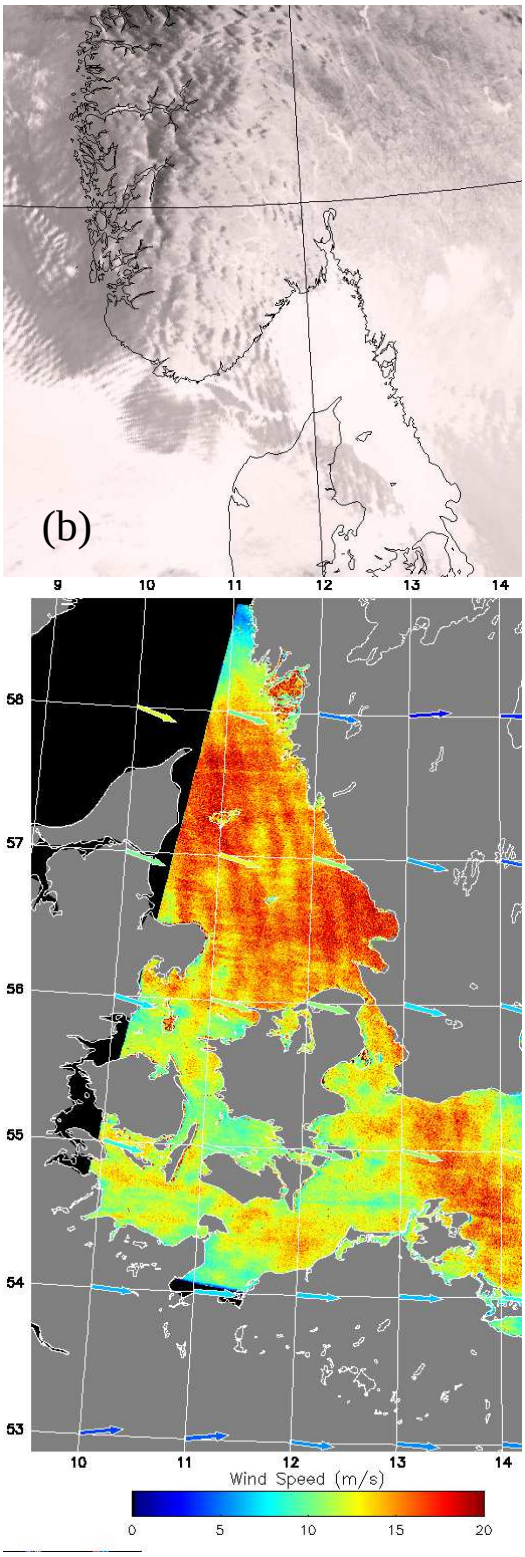

Figure 22: (above) Cloud picture (below) SAR image, showing the presence of gravity waves. From [38].

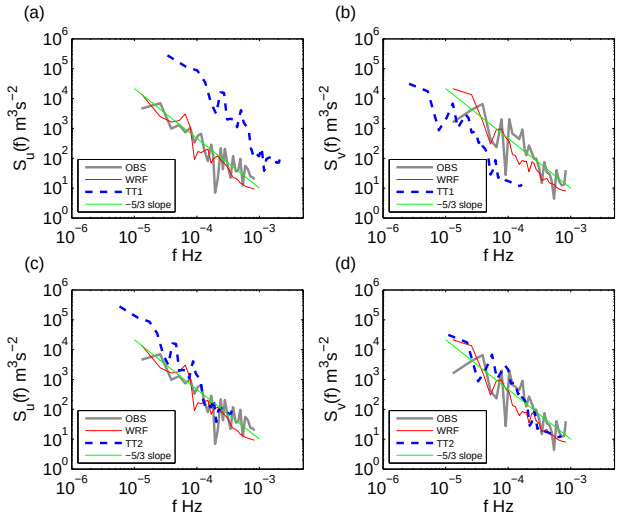

Figure 23: Temporal spectra of (a, c) u_{10} and (b,d) v_{10} for the day in the presence of gravity waves, 6 November, 2006. The solid curves are obtained directly from the time series of u_{10} and v_{10}, and the dashed curves from k-spectra. In (a,b), these are obtained through Eq. (21) (TT1) and in (c,d), these are through Eq. (20). From [38].

other hand, the co-spectrum for the v component decays exponentially with fd/U_0 but has a better correlation than the average curve for the stationary data. At the same time, the phase shift varies between -180° and 180° (Fig. 24b, e).

5.2.4 Open cells

Open cells, classified as type-I cloud-topped boundary layers by [40], frequently occur during cold air outbreaks [41]. Cold air advects over warm water, and becomes modified, leading to formation of clouds that frequently take the form of cloud street, roughly oriented along the winds in the outbreak. [35] observed that the cloud street transforms into three dimensional open cells further downwind in the outbreak.

Open cells are generated over water but can be advected over land, with the cell characteristics remained, see the Visual Satellite images in figure 5.11 in [42]. Open cells are frequently observed over the Danish water and they are shown to be a significant contributor to mesoscale wind variability at Horns Rev [42]. The extraordinary energy related with the open cells was shown in [29] with 18 cases from Horns Rev for the frequency range

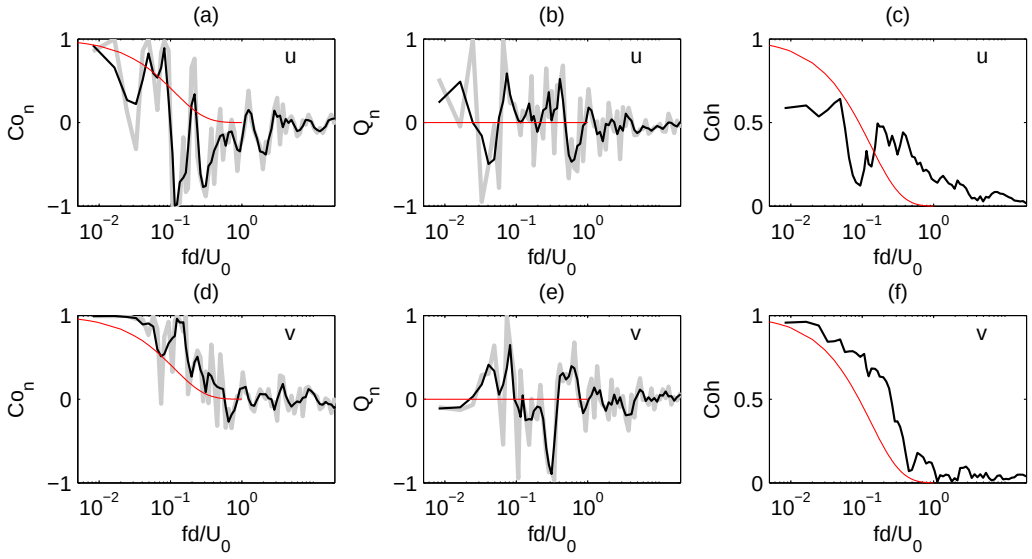

Figure 24: Co_n, Q_n and Coh between M_1 and M_3 at Nysted for the gravity wave case studied in [38]. The black curves are from the gray curves with running mean of three values. The thin smooth curves in (a,d) and (b,e) are respectively from Eq. (18) and (19) in V2012 corresponding to inflow angle $\alpha = 270°$ relative to the masts orientation (wind along with the $M_1 - M_3$ orientation). The smooth curves in (c,f) are $Coh = \exp[1.8\cos(2\alpha) - 5.9fd/U_0]$ with $\alpha = 270°$. From [29].

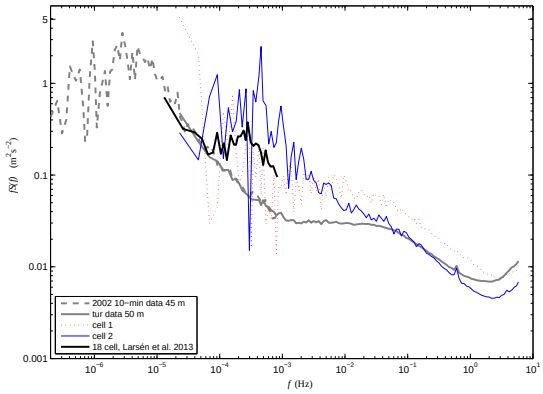

Figure 25: The spectra of wind speed at Horns Rev 1 M2 site. The think blue and dashed red curves are from two days when open cells are present. From [32].

$10^{-4} < f < 10^{-3}$ Hz through 10-min mean wind measurements; the mean spectrum for these 18 cases is copied here in Fig. 25 as the thick black curve. In [32], two such cases were shown through sonic measurements, suggesting that the contribution can modify the 3D turbulence substantially; they are reproduced here in Fig. 25.

To wind energy application, the challenge is the significant wind fluctuation associated with the open cells that are not taken into account in the standard calculations for turbulence and load. The fluctuation associated with such organized structures is also a challenge for power integration since it breaks down the normal spatial coherence description of the wind field.

The isotropy also breaks down in the mesoscale range in the presence of open cells, as analyzed in [29], see their Fig. 11 and 13. The u and v components are analyzed here during a two-day period when the open cells were present: 2011-12-03 and 2011-12-04 and the corresponding power spectra are shown in Fig. 26a and b for u and v, respectively. The data are from M8 at 107 m above sea level from Horns Rev II and unfortunately, the highest frequency available data here are 1-min mean values, so that the entire 3D turbulence can not be shown. The smooth curves in Fig. 26 are the Kaimal turbulence model with $z = 107$ m and $z_0 = 0.0001$ m. Apparently, both the u and v spectra contain significantly larger energy for $f < 0.005$ Hz, which can not be described by the Kaimal model.

Figure 27 shows the consistent spectral properties of the wind speed at Horns Rev M8 (107 m) and Høvsøre at 80 m. Earlier analysis suggests

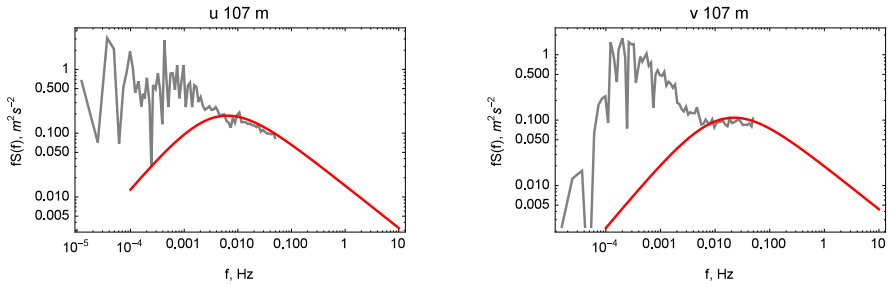

Figure 26: The spectra of the along wind component u (left) and the cross wind component v (right) at Horns Rev II M8 during a two-day period 2011-12-03 and 2011-12-04 when open cells are present. The data are 1-min mean wind from M8 in Horns Rev II at 107 m. The red curves are the Kaimal turbulence model.

that, even though Høvsøre met mast is on land, 80 m on the mast is mostly representing the offshore condition. Here the sonic measurements at Høvsøre are available and it can be seen that the Kaimal model describes well the turbulence for $f > 0.005$ Hz, in agreement with the case at Horns Rev M8.

In Fig. 28 the spectra from 10 m (blue) and 20 m (green) from Høvsøre are plotted on top of Fig. 27, together with the Kaimal model for the 3D turbulence. For $f < f_p$, where f_p is the peak frequency, the spectra behave as expected, with increasing f_p with height and decreasing level of energy. For $f < 0.005$ Hz, the spectra at all levels at Høvsøre are similar, being comparable to that at Horns Rev M8. The open cells are organized structures, horizontally (Horns Rev M8 and Høvsøre) and vertically (10 m to 107 m).

One direct consequence of not including the energy associated with the open cells is the underestimation of the turbulence intensity. This is shown in Figure 29 for the 2011-12-03 and 2011-12-04 open cell case for 10 m and 100 m, where the gray lines show the time series of the 10-min standard deviation of wind speed (σ_u) from measurements and the red lines show the calculated σ_u from the Kaimal spectrum for $10^{-3} < f < 1$ Hz. The underestimation of using the Kaimal model is obvious.

However, even the spectrum with the presence of open cells follows the idea as demonstrated in Fig. 16 and 17: that the contributions from different frequencies are uncorrelated or very weakly correlated. This is supported by Fig. 30 where it is shown that the sum of the 10-m Kaimal-type of spectrum (black) and the open cell fluctuation represented by the green line gives the red curve, which agrees with the measured spectrum in the intermediate frequency range.

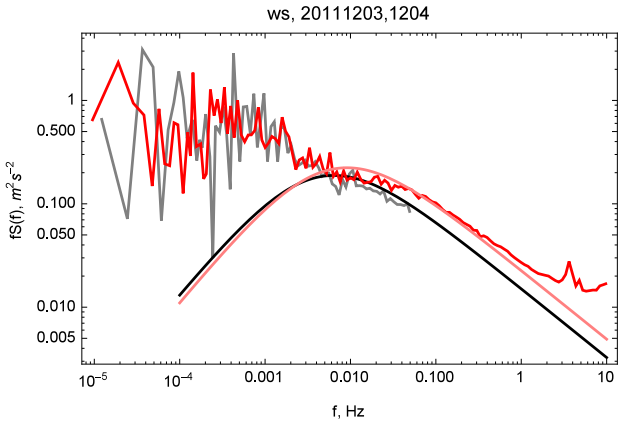

Figure 27: For the same period as in Fig. 26, the spectra of wind speed at Horns Rev M8 107 m (gray) and Horns Rev met mast 80 m (red). The black and pink curves are the Kaimal turbulence model for Horns Rev II and Høvsøre.

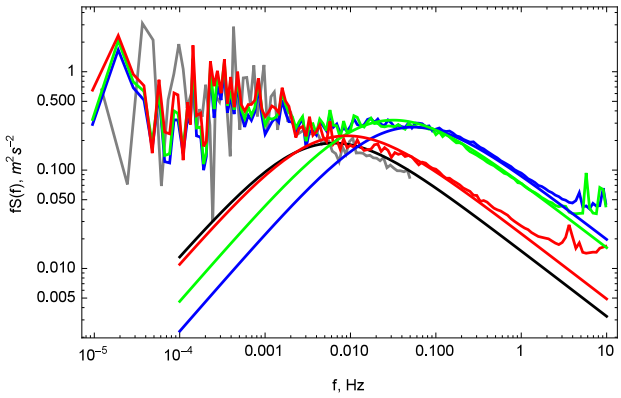

Figure 28: The gray and red curves are the same as in Fig. 27. Spectra from Høvsøre met mast 10 m (blue) and 20 m (green) are included. Again the smooth curves are the Kaimal model fitted to the measurements.

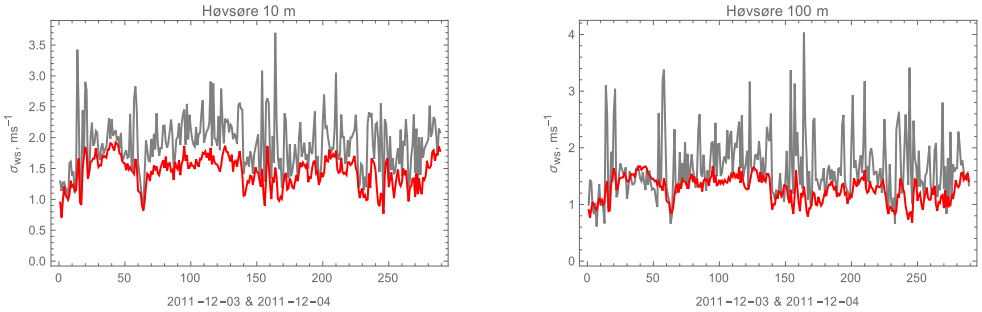

Figure 29: The standard deviation of wind speed (σ_u) at 10 m and 100 m. The gray lines are time series of 10-min σ_u from measurements which include the open cell fluctuations and the red lines are time series of 10-min σ_u where the mesoscale fluctuations are not included.

This is good news. If we could model the open cells to a resolution of about 10 min, with a Kaimal turbulence model we could reproduce the turbulence with the open cell contribution accounted.

In a study of extreme wave using the modeling system as described in 4.1 during 2006-11-01 over the North Sea, open cells were observed too, see the SAR image Fig. 10 [16]. The open cells shown in the SAR image seem to be reasonably modeled by the modeling system at a spatial resolution of 2 km, see Fig. 9b, which again in Fig. 31b shown as a good agreement in the spectra in wave number domain for $k < 3 \cdot 10^{-4}$ rad m^{-1} for their overlapping area. For higher wave number the modeled energy level drops rapidly, reflecting unresolved spatial wind variation for scales smaller than about 15 km, which is expected for WRF at a spatial resolution of 2 km due to the smoothing effects in numerical modeling [17]. Corresponding to the resolved resolution of 15 km, at the observed mean speed of 20 ms^{-1}, the corresponding temporal resolution is 750 s. Fig. 9a shows that the 10-min modeled time series of wind speed at FINO 1 gives comparable level of energy to the measurements. The modeled and measured time series can be found in Fig. 12.

5.3 Calculating Gust

In wind engineering, the gust is often calculated through the so-called Rise Theory. The peak factor k_p, defined in terms of the gust wind u_{gust}, the mean

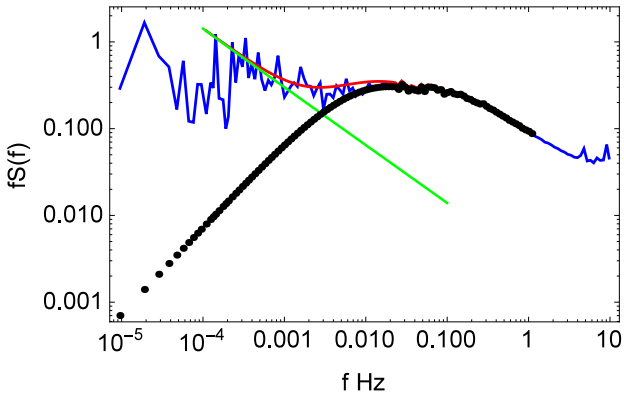

Figure 30: The spectra of wind speed in the presence of open cells from 2011-12-03 and 2011-12-04, at Høvsøre 10 m. The blue curve is calculated from the 2-day sonic measurements. The black curve for $f < 0.02$ Hz is a shape of the Kaimal model and measurements for $f > 0.02$ Hz. The green curve is simplified energy level responsible for mesoscale fluctuation for $f > 10^{-4}$ Hz. The red is the sum of Kamail spectrum plus the green spectrum.

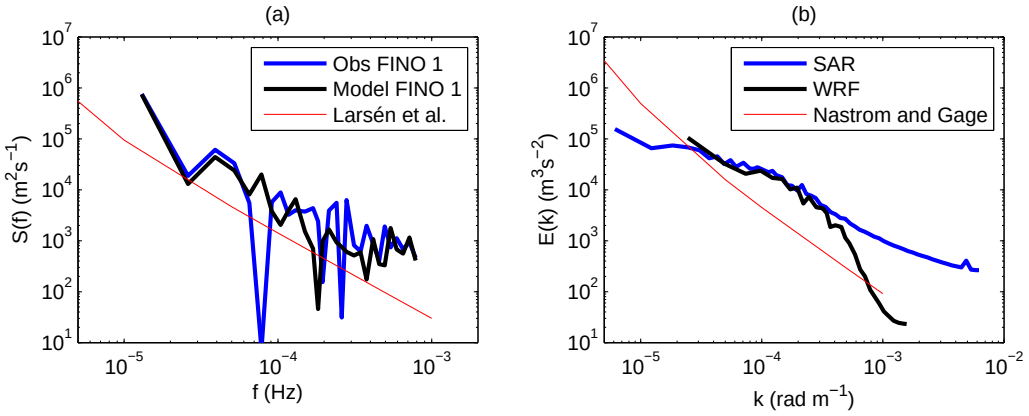

Figure 31: (a) At FINO 1, power spectra of wind speed at 100 m from measurements and modeling. The red curve is the climatological from [29]. (b) Spectra in wave number domain, from SAR winds and modeled wind for the overlapping area of Fig. 10 and Fig. 9b. The red curve is the k-spectrum from [43]. From [16].

wind u_{mean} and the standard deviation σ:

$$k_p = \frac{u_{gust} - u_{mean}}{\sigma}, \tag{22}$$

can be calculated through

$$k_p = \sqrt{2\ln(\nu t_0)} - \frac{\gamma}{\sqrt{2\ln(\nu t_0)}} \tag{23}$$

where $\gamma = 0.577$ is the Eular's constant, t_0 is the basis period of the time series used for calculating the gust, and $\nu = \sqrt{\frac{m_2}{m_0}}$, with the zero- and second-order spectral moments m_0 and m_2 calculated through:

$$m_j = \int_{\omega_1}^{\omega_2} \omega^j S(\omega) d\omega, \tag{24}$$

where $\omega = 2\pi f$, ω_1 and ω_2 are the starting and ending frequencies for the integration. ω_1 is normally taken as $(10\ \text{min})^{-1}$ or $1\ \text{h}^{-1}$, and ω_2 is the resolution that the gust is to be calculated to, i.e. 1 s or 3 s gust. The choice of $(10\ \text{min})^{-1}$ or $1\ \text{h}^{-1}$ is related to the turbulence gap theory where the 3D turbulence becomes negligible at the spectral gap. For $S(\omega)$, the Kaimal model and the Mann model are two of the often used.

This theory for gust calculation has shown to be working well in the atmospheric surface layer. In storm conditions, the boundary layer and hence the surface layer (SL) can reach a quite high level, for instance for SL height of 100 m above the ground. At elevations above the surface layer, as many modern turbines are, the power spectrum $S(\omega)$ can no longer be described by the surface parameters such as z_0 and u_*. Limitations are also expected when, even very close to the surface, the turbulence can be significantly modified by the organized structures such as shown in Fig. 28 and 30. Both situations are challenged by large scale flow modification of the local turbulence.

One solution would be to solve the turbulence spectrum for the lower frequencies. However, there is a theory proposed by Brasseur [44] in which the occurrence of gust at the surface is through a non-local process. It is produced by the deflection of air parcels flowing in the boundary layer and brought down to the surface through turbulent eddies. This theory argues that an air parcel will be able to reach the surface if the vertical component of the turbulence kinetic energy (TKE) is strong enough to counteract the buoyancy force. The gust at the surface is then taken as the largest winds over the vertical model levels where averaged TKE is greater than the averaged buoyancy force.

The Brasseur's theory has been applied in DTU's South Africa Wind Atlas project and an atlas of the 50-year 3-s gust winds has been published

in e.g. [11] and [12]; Fig. 32 is a copy where Fig. 32a is based on measurements from 70 stations across the country, Fig. 32b and c are from the modeling. In this project we used WRF modeling at a spatial resolution of 4 km and a time step of 20 s. More than 250 storms were modeled for the period from 1998 to 2010 over Western and Eastern Cape in South Africa. The MYNN planetary boundary layer scheme was used in our WRF modeling. The vertical profiles of TKE and buoyancy were calculated in WRF and used to apply the Brasseur method. Figure 33 shows an example of the gust calculation using this non-local gust theory during one storm event at a Cape Town station together with measured 3-s gust values at 10 m. It is difficult to quantify the comparison due to several factors. Firstly, the modeling time step is 20 s, which is not necessarily corresponding to a temporal resolution of 20 s. With a mesoscale modeling, straightforwardly increasing the temporal or spatial resolution will not necessarily help resolving finer scale flow movement. Therefore, it is not easy to obtain a 3 s gust through a mesoscale modeling. Secondly, the measured gust values at e.g. 10 m are affected by the surface conditions. However, in the Brasseur theory, such a local effect is not included. What we obtained through this theory is most valid for higher elevations. These might help interpreting the difference between the modeled and measured gust values in Fig. 33. Nevertheless, the modeled time series of the gust value does follow that of the measured one with comparable magnitude, which supports the non-local gust concept. In [12] this method was also applied to the storms over Denmark and validated with measurements from Høvsøre. It was found that the gust estimates from the Brasseur method using WRF agree better with measurements at higher levels such as 80 m and 100 m than at lower levels such as 10 m and 20 m.

This method is applied for storm Britta too when the open cells are present. Figure 34a and b shows the underestimation of the use of a classical turbulence model for the gust estimation (black curves) in comparison with measurements from Høvsøre at 10 m and 80 m. Here the 10-min time series of the 3-s gust are shown for the two days 2006-10-31 00:00 to 2006-11-01 23:50. Figure 34c shows the modeled gust, although there needs improvement for the storm phase for the first 50 ten minutes, the gust magnitude is more comparable to the measured values than using Kaimal turbulence model. Note the two gray curves are the upper and low bounds of the gust within the Brasseur method.

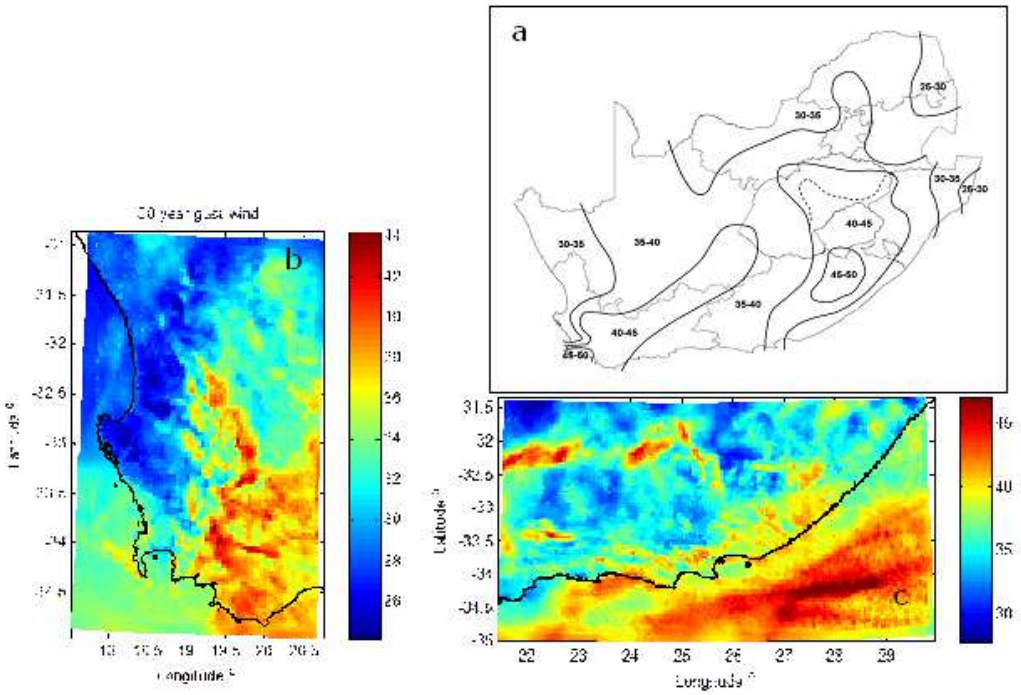

Figure 32: Atlases of the 50-year gust wind. (a) From measurements. (b) Over Western Cape, using WRF, Brasseur method and Annual Maximum Method. (c) Similar to (b) but over Eastern Cape. From [12].

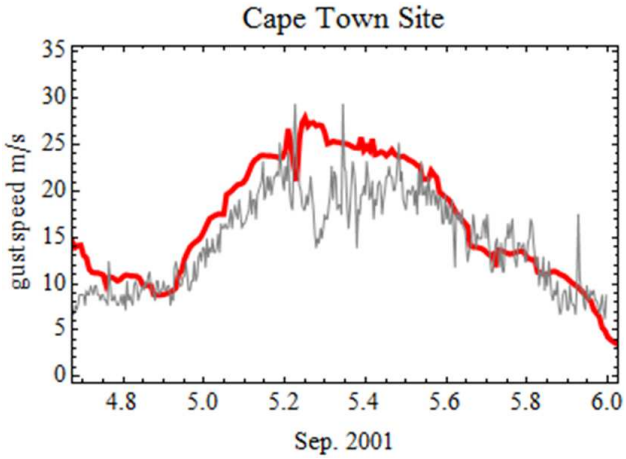

Figure 33: Time series of the measured (gray) and modeled (red) gust wind at 10 m at Cape Town met station during one storm in 4th - 6th Sep. 2001. From [12].

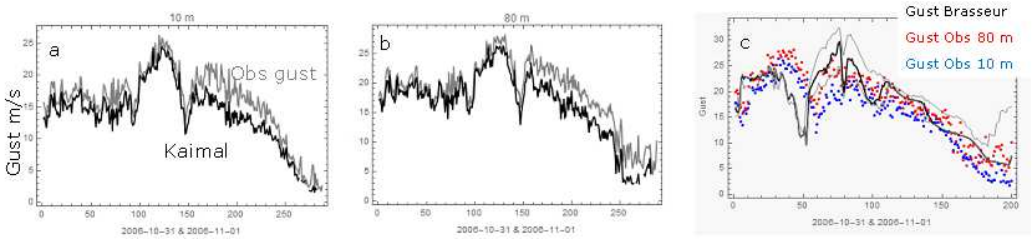

Figure 34: (a) Time series of the measured and modeled gust using Kaimal turbulence model at Høvsøre at 10m. (b) Similar to (a) but at 80 m. (c) Comparison of the Brasseur method using WRF with measured gusts at 10 m and 80 m. The gray curves in (c) are the upper and low bounds for gust in the Brasseur method.

6 Summary

This report collects and analyzes our ongoing researches on offshore meteorological and oceanic conditions in the context of offshore applications such as design, operation and maintenance.

The wind-wave coupled modeling system can be used for forecasting where the outputs are time series of meteorological and oceanic parameters over the space, such as wind speed, direction, vertical wind profile, significant wave height, wave length and wave direction.

The modeling system can also be used for hindcasting where a climate of storm winds and waves can be obtained through a reproduction of hundreds of storms. One application of the such a reproduction of storm climate is the estimate of the extreme winds and extreme waves. The method developed at DTU Wind Energy efficiently collects and downscales meaningful storms in relation to the statistical approach for the extreme value estimate, the Annual Maximum Method.

In addition to the storm episodes method for the extreme wind, the spectral correction method was developed for extremes over relative simple terrains in connection with the use of climatological data sets. The climatological data usually miss the variation due to model smoothing effect, which results in general underestimation of extreme values. This method feeds in the missing variation based on studies of measurements.

Our studies demonstrate the importance of the turbulence of larger scales. The spectral correction method is one of the examples. Studies of larger scale

wind variations and spatial coherence are also relevant for power integration; both numerical modeling and measurement analysis are shown to be useful for obtaining the relevant information.

Strong winds occur rather frequently over the North Sea. In connection with these strong wind events, organized structures such as gravity waves, boundary layer rolls and open cells are often present over the water and propagate over land. These mesoscale features have their own temporal and spatial characteristics, modifying the climatological power spectra and spatial coherence of the wind field, and the impact related should be evaluated in connection with many of our existing calculations in wind energy applications, such as load, gust and integration.

References

[1] J. C. Warner, B. Armstrong, R. He, and J. Zambon. Development of a coupled ocean-atmosphere-wave-sediment transport (COAWST) modeling system. *Ocean Modeling*, 35:230–244, 2010.

[2] N. Booij, R.C. Ris, and L. H. Holthuijsen. A third-generation wave model for coastal regions: 1. model description and validation. *J. Geophys. Res. doi:10.1029/98JC02622*, 104(C4):7649, 1999.

[3] H. Charnock. Wind stress on a water surface. *Q. J. R. Meteorol. Soc.*, 81:639–640, 1955.

[4] W. Drennan, J. A. Zhang, J. F. French, C. McCormick, and P. G. Black. Turbulent fluxes in the hurricane boundary layer. Part II: latent heat flux. *Journal of Atmospheric Sciences*, 64:1103–1115, 2007.

[5] Y. Fan, S. Lin, I. M. Held, Z. Yu, and H. L. Tolman. Global ocean surface wave simulation using a coupled atmosphere-wave model. *Journal of Climate*, 25:6233–6252, 2012.

[6] B. Liu, H. Liu, L. Xie, C. Guan, and D. Zhao. A coupled atmosphere-wave-ocean modeling system: simulation of the intensity of an idealized tropical cyclone. *Monthly Weather Review*, 139:132–152, 2011.

[7] W.A. Oost, G. J. Komen, C. Jacobs, and C. Van Oort. New evidence for a relation between wind stress and wave age from measurements during ASGAMAGE. *Boundary-layer Meteorol.*, 102:409–438, 2002.

[8] P.A.E.M. Janssen. Quansi-linear theory of wind generation applied to wave forecasting. *Journal of Physical Oceanography*, 21:1631–1642, 1991.

[9] J. Du, R. Bolaños, and X. G. Larsén. The use of a wave boundray layer model in SWAN. *Journal of Geophysical Research - Ocean, in press*, 2016.

[10] X. G. Larsén, J. Badger, A. N. Hahmann, and N. G. Mortensen. The selective dynamical downscaling method for extreme-wind atlases. *Wind Energy*, 16:1167–1182, 2013.

[11] A. Otto. *WASA: The wind atlas for South Africa Project, Phase I.* Impumelelo Print Solutions (Pty) Ltd, 2015.

[12] X. G. Larsén and A. Kruger. Extreme gust wind estimation using mesoscale modeling. In: Scientific Proceedings. EWEA 2014 Barcelona. 2014.

[13] X.G. Larsén. Extreme wind mapping over the north sea. Technical Report Wind Energy Report-I-0047, Wind Energy Department, DTU, Roskilde, Denmark, 2013.

[14] A.C. Kruger, J. Retief, A. Goliger, and X.G. Larsén. Optimal application of climate data to the development of design wind speeds. *Proceedings of 94th American Meteorological Society Annual Meeting, American Meteorological Society*, 2014.

[15] X. G. Larsén and A. Kruger. Application of the spectral correction method to reanalysis data in South Africa. *J. Wind Eng. Ind. Aerodyn.*, 133:110–122, 2014.

[16] X. G. Larsén, J. Du, R. Bolaños, and S. Larsen. Storm Britta Revisted. *Ocean Dynamics, submitted*, 2016.

[17] W.C. Skamarock. Evaluating mesoscale NWP models using kinetic energy spectra. *Mon Weather Rev*, 132:3019–3032, 2004.

[18] W.C. Skamarock. Kinetic energy spectra and model filters. *Lecture Note in Numerical Techniques for Global Atmospheric Models*, 80:495–512, 2011.

[19] R. Frehlich and R. Sharman. The use of structure functions and spectra from numerical model output to determine effective model resolution. *Monthly Weather Rev.*, 136:1537–1553, 2008.

[20] X. G. Larsén, A. Kruger, J. Badger, and H. Jørgensen. Extreme wind atlases of South Africa from global reanalysis data. In: Scientific Proceedings (on line). European-African Conference of Wind Engineering, Cambridge, UK. 2013.

[21] X. G. Larsén, S. Ott, J. Badger, A. H. Hahmann, and J. Mann. Recipes for correcting the impact of effective mesoscale resolution on the estimation of extreme winds. *J. Appl. Meteorol. Climat.*, 51(3):521–533, 2012.

[22] B. O. Hansen, X. G. Larsén, M. Kelly, O. S. Rathmann, J. Berg, A. Bechmann, A. M. Sempreviva, and H. E. Jørgensen. Extreme wind calculation applying spectral correction method - test and validation. Techni-

cal report, Wind Enery Department, Technical University of Denmark, DTU Wind Energy E-0098, 2016.

[23] X. G. Larsén, C. Kalogeri, G. Galanis, and G. Kallos. A statistical methodology for the estimation of extreme wave conditions for offshore renewable applications. *Renewable Energy*, 80:205–218, 2015.

[24] H. K. Johnson, H.J. Vested, H. Hersbach, J. Højstrup, and S.E. Larsen. The coupling between wind and waves in the WAM model. *Journal of atmospheric and oceanic technology*, 16:1780–1790, 1999.

[25] P. Pilar, C. G. Soares, and J.C. Carretero. 44-year wave hindcast for the North East Atlantic European coast. *Coastal Engineering*, 55:861–871, 2008.

[26] A.W. Ratsimandresy, M.G. Sotillo, J.C. Carretero Albiach, E. Álvarez Fanjul, and H. Hajji. A 44-year high-resolution ocean and atmospheric hindcast for the Mediterranean Basin developed within the HIPOCAS Project. *Coastal Engineering*, 55:827–842, 2008.

[27] J.C. Kaimal and J.J. Finnigan. *Atmospheric boundary layer flows*. Oxford University Press, New York, 289 pp, 1994.

[28] J. Mann. The spatial structure of neutral atmospheric surface-layer turbulence. *J. Fluid Mech.*, 273:141–168, 1994.

[29] X. G. Larsén, C. L. Vincent, and S. Larsen. Spectral structure of the mesoscale winds over the water. *Q. J. R. Meteorol. Soc.*, 139:685–700, 2013.

[30] U. Högström, J.C.R. Hunt, and A.-S. Smedman. Theory and measurements for turbulence spectra and variances in the atmospheric neutral surface layer. *Boundary-Layer Meteorol*, 103:101–124, 2002.

[31] K.C. Kim and R.J. Adrian. Very large-scale motion in the outer layer. *Phys Fluids*, 11:417–422, 1999.

[32] X. G. Larsén, S. E. Larsen, and E. L. Petersen. Full-Scale Spectrum of Boundary-Layer Meteorology. *Boundary-Layer Meteorology*, 159:349–371, 2016.

[33] E.L. Petersen, X. G. Larsén, and S. Larsen. The model chain and the full scale horizontal wind spectrum of the boundary layer wind. *Proceedings WindEurope 2016, Risø campus, DTU Wind Energy*, 2016.

[34] Van der Hoven. Power spectrum of horizontal wind speed in the frequency range from 0.0007 to 900 cycles per hour. *J. Meteorol.*, 14:160–164, 1957.

[35] B. Brümmer. Roll and cell convection in wintertime Arctic cold-air outbreaks. *Journal of the Atmospheric Sciences*, 56:2613 – 2636, 1999.

[36] A.-S. Smedman. Occurrence of roll circulation in a shallow boundary layer. *Boundary-Layer Meteorol*, 51:343–358, 1991.

[37] X. G. Larsén, S. Larsen, and A. Hahmann. Origin of the waves in "a case study of mesoscale spectra of wind and temperature, observed and simulated': Lee waves from the norwegian mountains'. *Q. J. R. Meteorol. Soc.*, 138:274–279, 2012.

[38] X. G. Larsén, S. Larsen, and M. Badger. A case study of mesoscale spectra of wind and temperature, observed and simulated. *Q. J. R. Meteorol. Soc.*, 137:264–274, 2011.

[39] C. J. Nappo. *An introduction to atmospheric gravity waves.* Academic Press, 2002.

[40] E.M. Agee. Meso-scale cellular convection over the oceans. *Dyn. Atmos. Ocean.*, 10:317–341, 1987.

[41] B. W. Atkinson and J. W. Zhang. Mesoscale shallow convection in the atmosphere. *Reviews of Geophysics*, 4:403–431, 1996.

[42] C. L. Vincent. Mesoscale wind fluctuations over Danish waters. Technical Report Risø-PhD-70(EN), Risø DTU, National Laboratory for Sustainable Energy, Roskilde, Denmark, 2010.

[43] G.D. Nastrom and K.S. Gage. A climatology of atmospheric wavenumber spectra of wind and temperature observed by commercial aircraft. *J. Atmos. Sci*, 42:950–960, 1985.

[44] O. Brasseur. Development and application of a physical approach to estimating wind gusts. *Monthly Weather Review*, 129:5–25, 2001.